

A δf PIC method with auxiliary Forward-Backward Lagrangian reconstructions

Martin Campos Pinto¹, Merlin Pelz¹, and Pierre-Henri Tournier²

¹Max-Planck-Institut für Plasmaphysik, Garching, Germany

²Sorbonne Université, CNRS, Université de Paris, Laboratoire Jacques-Louis Lions (LJLL), F-75005 Paris, France

October 10, 2022

Abstract

In this note we describe a δf particle method where the bulk density is periodically remapped on a coarse spline grid using a Forward-Backward Lagrangian (FBL) approach. We describe the method in the case of an electrostatic PIC scheme and validate its qualitative properties using a classical two-stream instability subject to a uniform oscillating drive.

1 Introduction

In order to reduce the statistical noise in numerical simulations of kinetic plasma problems, particle methods often follow a so-called δf approach [11, 8, 14] which consists of decomposing the transported density in two parts, a bulk density f_0 given by an analytical formula and a variation δf represented with numerical particles. In [2] this approach was revisited as a variance reduction method in the scope of Monte Carlo algorithms, with f_0 playing the role of a control variate, and since then several techniques have been devised to improve the reduction of statistical error, in particular for Gyrokinetic [10, 13, 12, 9] and collisional models [5, 19, 18].

In many practical problems where the plasma remains close to an equilibrium state, the total density deviates only slightly from its initial profile which is then used as a constant bulk density. In some case however the deviation grows in time and f_0 needs to be updated to better follow the total density. For such cases an attractive scheme, which consists in projecting the particle density δf on a coarse spline basis, has been proposed in [1].

In this article we consider a variant of this method where the bulk density is evolved using a semi-Lagrangian approach based on the Forward-Backward Lagrangian (FBL) method [4]. As the latter relies on periodic reconstructions of the characteristic backward flow using a set of markers that have been pushed forward along precise trajectories, coupling the δf and FBL approaches appears as a natural option for practical applications.

The outline is as follows. In Section 2 we present our general ansatz for the discrete density, which may be seen as a hybrid discretization between particle and semi-lagrangian density representations. In Section 3 we then recall the key steps of electrostatic particle-in-cell approximations, and in Section 4 we describe the δf PIC method with FBL remappings of the

bulk density. The proposed method is summarized in Section 5, and in Section 6 we present a series of numerical results involving two-stream instability test cases to illustrate the enhanced denoising properties of our approach.

2 Approximation ansatz

Our ansatz for the density at a discrete time t^n is a sum of two terms,

$$f^n := f_*^n + \delta f^n \quad (1)$$

where the first one will be seen as the bulk density, a smooth approximation to the full solution, and the second one as the fine scale variations. Following the general principle of δf methods we require f_*^n to have a simple expression that is easy to evaluate at arbitrary positions of the phase space, and we represent the variation δf^n as an unstructured collection of numerical particles,

$$\delta f^n(z) = \sum_{k=1}^{N_p} \delta w_k^n \varphi_\varepsilon(z - z_k^n) \quad (2)$$

where φ_ε is a smooth shape function of scale ε and $z = (x, v)$ is the phase-space coordinate. In typical problems where the transported density slightly deviates from an initial profile, the bulk density is often set to this initial value, $f_*^n = f^0$. In this note we investigate an alternate approach similar to [1] and represent the bulk density as a spline approximation on a coarse grid with mesh-size $h_* > \varepsilon$. This yields an expression that is formally similar to that of δf^n ,

$$f_*^n(z) = \sum_{\mathbf{j} \in \mathbb{Z}^d} w_{*,\mathbf{j}}^n \varphi_{h_*}(z - \mathbf{j}h_*) \quad (3)$$

where $\varphi_*(\cdot - \mathbf{j}h_*)$ are now coarse B-spline shapes centered on the grid nodes. In practice, only a finite number N_* of such nodes is used, and as outlined in the introduction we will periodically update the coefficients of this spline bulk density using a Forward-Backward Lagrangian (FBL) reconstructions, which involves a relatively small set of passive markers designed to track the characteristic flow in phase space and periodically remapped on the coarse structured grid.

2.1 Main numerical parameters and limit regimes

The main numerical parameters are as follows.

- N_r is the remapping period, i.e. the number of time steps between two updates of the bulk density. The limit value $N_r = \infty$ corresponds to a frozen bulk density, namely $f_*^n = f_*^0$.
- N_* is the number of coarse splines used to represent the bulk density, in a bounded domain $\Omega \subset \mathbb{R}^d$ it is on the order of $|\Omega|(h_*)^{-d}$. The limit value of $N_* = 0$ (an empty grid) corresponds to a “full- f ” particle approximation.
- N_p is the number of numerical particles describing the fine scale structures. The limit value of $N_p = 0$ corresponds to a semi-Lagrangian ansatz [17] where the full density is represented on a structured grid and can be updated in time with an ad-hoc scheme such as the FBL method described in [4].

2.2 Weighted collections of spline shape functions

For simplicity, we consider spline shape functions for both the bulk density and the fine scale variations. Specifically, we set

$$\varphi_\varepsilon(z) = \left(\frac{1}{\varepsilon}\right)^d \varphi\left(\frac{z}{\varepsilon}\right), \quad z \in \mathbb{R}^d$$

with a reference shape function φ defined as a centered cardinal B-spline of degree p ,

$$\varphi(z) := \prod_{i=1}^d B_p(z_i) \quad \text{with support} \quad \text{supp}(\varphi) = \left[-\frac{p+1}{2}, \frac{p+1}{2}\right]^d \quad (4)$$

involving standard univariate B-splines $B_0(x) = \mathbb{1}_{[-\frac{1}{2}, \frac{1}{2}]}(x)$ and $B_p(x) = \int_{x-\frac{1}{2}}^{x+\frac{1}{2}} B_{p-1}$ for $p \geq 1$. In the sequel, it will be convenient to denote an arbitrary collection of weighted splines as

$$\Phi_\varepsilon[\mathbf{W}, \mathbf{Z}](z) := \sum_{k=1}^N w_k \varphi_\varepsilon(z - z_k) \quad \text{where} \quad \mathbf{W} = (w_k)_{k=1\dots N}, \quad \mathbf{Z} = (z_k)_{k=1\dots N}. \quad (5)$$

With this convention, the two components of our general ansatz (1) read

$$f_*^n = \Phi_{h_*}[\mathbf{W}_*^n, \mathbf{Z}_*^n] \quad \text{and} \quad \delta f^n = \Phi_\varepsilon[\delta \mathbf{W}^n, \mathbf{Z}^n] \quad (6)$$

where $\mathbf{Z}_* = (j h_*)_{j \in \mathbb{Z}^d}$ are the nodes of the structured spline grid.

3 Particle approximations to transport equations

Our method may be described for general non-linear transport problems of the form

$$\partial_t f(t, z) + U[f] \cdot \nabla_z f(t, z) = 0 \quad (7)$$

where $z \in \mathbb{R}^d$ is the phase-space variable and $U[f]$ the generalized velocity field associated to the solution f .

3.1 Characteristic flows

The characteristic trajectories associated to (7) are the curves $\mathcal{Z}(t) = \mathcal{Z}(t; s, z)$, solution to the ODEs

$$\frac{d}{dt} \mathcal{Z}(t) = U[f](t, \mathcal{Z}(t)), \quad \mathcal{Z}(s) = z$$

for arbitrary $s, t \in [0, T]$ and $z \in \mathbb{R}^d$, see e.g. [15]. The (forward) characteristic flow between two instants $t^n = n\Delta t$ and t^{n+1} is then defined as

$$\mathcal{F}_{\text{ex}}^{n, n+1} : \mathbb{R}^d \rightarrow \mathbb{R}^d, \quad z \mapsto \mathcal{Z}(t^{n+1}; t^n, z) \quad (8)$$

and the inverse mapping is the backward flow

$$\mathcal{B}_{\text{ex}}^{n, n+1} = (\mathcal{F}_{\text{ex}}^{n, n+1})^{-1} : z \mapsto \mathcal{Z}(t^n; t^{n+1}, z). \quad (9)$$

Using the backward flow we can write the solution to (7) over the time interval $[t^n, t^{n+1}]$, as

$$f(t^{n+1}, z) = f(t^n, \mathcal{B}_{\text{ex}}^{n, n+1}(z)). \quad (10)$$

Here we may restrict ourselves to divergence-free velocity fields: $\text{div}_z U[f] = 0$. The characteristic flows are then measure-preserving and the transport is conservative.

3.2 1D1V Vlasov-Poisson equation

A simple example is the periodic 1D1V Vlasov-Poisson equation

$$\partial_t f(t, x, v) + v \partial_x f(t, x, v) - E(t, x) \partial_v f(t, x, v) = 0, \quad t \geq 0, (x, v) \in [0, L] \times \mathbb{R}, \quad (11)$$

with a normalized initial density $\int_0^L \int_{\mathbb{R}} f^0(x, v) dv dx = 1$ and a periodic electric field $E = E[f]$ defined by

$$\begin{cases} E(t, x) = -\partial_x \phi(t, x) \\ -\Delta \phi(t, x) = \rho(t, x) = \frac{1}{L} - \int_{\mathbb{R}} f(t, x, v) dv. \end{cases} \quad (12)$$

This corresponds to an electrostatic, normalized ($\varepsilon_0 = q = m = 1$) periodic electron plasma in 1d, with constant neutralizing background ion density, so that $\int_0^L \rho dx = 0$. Here the generalized velocity field is

$$U[f](t, z) = (v, -E(t, x)) \quad \text{with } z = (x, v).$$

Due to the non-linear nature of this transport equation, the characteristic flow has no explicit expression.

3.3 Full- f particle approximation

Particle approximations represent the transported density $f^n(z) \approx f(t^n)$ as a sum of numerical particles of the form

$$f^n(z) = \Phi_\varepsilon[\mathbf{W}^n, \mathbf{Z}^n](z) \quad (13)$$

with weights initially set to

$$w_k^0 := \frac{f^0(z_k^0)}{N_p g^0(z_k^0)}, \quad k = 1, \dots, N_p, \quad (14)$$

where g^0 is the sampling distribution of the initial markers $\mathbf{Z}^0 = (z_k^0)_{k=1, \dots, N_p}$, see e.g. [18]. As the problem is conservative the weights are kept constant in time, $\mathbf{W}^{n+1} = \mathbf{W}^n$, and the markers are pushed forward

$$\mathbf{Z}^{n+1} = \mathcal{F}^n(\mathbf{Z}^n) \quad (15)$$

using some approximation to the forward flow (8) which takes as parameter the numerical solution at time t^n ,

$$\mathcal{F}^n(\mathbf{Z}) = \mathcal{F}_{\Delta t}[\mathbf{W}^n, \mathbf{Z}^n](\mathbf{Z}).$$

3.4 Electrostatic full- f leap-frog flow

For the Vlasov-Poisson equation (11), a standard numerical flow is given by a leap-frog (Strang splitting) scheme,

$$\mathcal{F}_{\Delta t, \Delta x}^{\text{lf, pic}}[\mathbf{W}^n, \mathbf{Z}^n](\mathbf{Z}) = \mathcal{F}_{\frac{\Delta t}{2}}^x \circ \mathcal{F}_{\Delta t, \Delta x}^{\text{v, pic}}[\mathbf{W}^{n+\frac{1}{2}}, \mathbf{Z}^{n+\frac{1}{2}}] \circ \mathcal{F}_{\frac{\Delta t}{2}}^x(\mathbf{Z}) \quad (16)$$

associated with a grid with M points and step-size $\Delta x = L/M$. The first split flow reads

$$\mathcal{F}_{\frac{\Delta t}{2}}^x : (x, v) \mapsto (x + \frac{\Delta t}{2} v, v) \quad (17)$$

and the second takes the form

$$\mathcal{F}_{\Delta t, \Delta x}^{\text{v,pic}}[\mathbf{W}^{n+\frac{1}{2}}, \mathbf{Z}^{n+\frac{1}{2}}] : (x, v) \mapsto (x, v - \Delta t E^{n+\frac{1}{2}}(x)). \quad (18)$$

Here we have set

$$\mathbf{W}^{n+\frac{1}{2}} := \mathbf{W}^n, \quad \mathbf{Z}^{n+\frac{1}{2}} := \mathcal{F}_{\frac{\Delta t}{2}}^{\text{x}}(\mathbf{Z}^n) \quad (19)$$

and the electric field is computed from the particles with a discrete Poisson solver such as the one described just below, that takes as input the particle weights and positions,

$$E^{n+\frac{1}{2}}(x) := \mathbb{E}_{\Delta x}^{\text{pic}}[\mathbf{W}^{n+\frac{1}{2}}, \mathbf{Z}^{n+\frac{1}{2}}](x). \quad (20)$$

3.5 Electrostatic full- f PIC field solver

To clarify how the particles are coupled with the field in (20), we recall the precise form of a basic Finite Difference (FD) Poisson solver for a general collection of weighted particles, i.e.

$$\Phi_\varepsilon[\mathbf{W}, \mathbf{Z}] \mapsto \mathbb{E}_{\Delta x, \varepsilon}^{\text{pic}}[\mathbf{W}, \mathbf{Z}]. \quad (21)$$

We note that for periodic systems spectral solvers involving fast Fourier transforms are often used, see e.g. [3, Sec. 8]. In both cases the charge deposition algorithm consists of computing grid values for the charge density,

$$\rho_i = \frac{1}{L} - \int_{\mathbb{R}} \Phi_\varepsilon[\mathbf{W}, \mathbf{Z}](i\Delta x, v) \, dv = \frac{1}{L} - \sum_{k=1}^{N_p} w_k \varphi_\varepsilon(i\Delta x - x_k) \quad \text{for } i = 1, \dots, M. \quad (22)$$

A discrete Poisson equation is then solved. With a FD scheme this reads

$$E_i = -\frac{\phi_{i+1} - \phi_{i-1}}{2\Delta x}, \quad -\frac{\phi_{i+1} - 2\phi_i + \phi_{i-1}}{\Delta x^2} = \rho_i, \quad \text{for } i = 1, \dots, M.$$

The electric field (21) is then defined using the same spline shape functions as the particles but a different normalization, and scaled with the FD grid:

$$\mathbb{E}_{\Delta x, \varepsilon}^{\text{pic}}(x) := \sum_{i=1}^M E_i \tilde{\varphi}_{\Delta x}(x - i\Delta x) \quad \text{where} \quad \tilde{\varphi}_{\Delta x}(x) = \varphi\left(\frac{x}{\Delta x}\right). \quad (23)$$

In the usual case where $\varepsilon = \Delta x$, we may simply write $\mathbb{E}_{\Delta x}^{\text{pic}} = \mathbb{E}_{\Delta x, \Delta x}^{\text{pic}}$.

4 A δf PIC scheme with remappings

We now describe the main steps of a δf method involving a decomposition of the form (1). Denoting by N_r the remapping period, we first observe that the bulk part is frozen between two remapping steps. This yields in particular

$$f_*^n = f_*^m \quad \text{where} \quad m = m(n) := \left\lfloor \frac{n}{N_r} \right\rfloor N_r. \quad (24)$$

The δf part is then evolved as follows.

4.1 δf particle approximation: basic steps

A typical δf time step consists of (i) pushing the markers forward to follow the characteristic curves as in (15),

$$\mathbf{Z}^{n+1} = \mathcal{F}^n(\mathbf{Z}^n) \quad (25)$$

and (ii) updating the weights. Indeed, since the numerical particles now represent a variation $\delta f^n = f^n - f_*^n$ with frozen f_*^n on the time step, their weights no longer carry a conserved density and they must be evolved in time. In the *direct* δf method (see e.g. [18, Sec. 3]) they are set as

$$\delta w_k^n := \frac{f_k^n - f_*^n(z_k^n)}{N_p g_k^n} \approx \frac{\delta f(t^n, z_k^n)}{N_p g(t^n, z_k^n)}, \quad k = 1, \dots, N_p \quad (26)$$

where

$$f_k^n \approx f(t^n, z_k^n) \quad \text{and} \quad g_k^n \approx g(t^n, z_k^n) \quad (27)$$

correspond to the transported density and the markers density probability, respectively, evaluated at the particle positions. Since both values are constant along exact trajectories, a reasonable choice is

$$f_k^n := f^0(z_k^0) \quad \text{and} \quad g_k^n := g^0(z_k^0). \quad (28)$$

Up to these constant values we see that the δf weights only depend on the bulk density, which is characterized by the weights $\mathbf{W}_*^n = \mathbf{W}_*^m$, at the marker positions \mathbf{Z}^n . Hence we may summarize the weighting scheme (26)–(28) as

$$\delta \mathbf{W}^n := \delta \mathcal{W}(\mathbf{W}_*^m, \mathbf{Z}^n). \quad (29)$$

4.2 Electrostatic δf -PIC flow

In the case of a δf ansatz, the leap-frog flow reads

$$\mathcal{F}_{\Delta t, \Delta x}^{\text{lf}, \delta f}[\mathbf{W}_*^m, \mathbf{Z}^n] = \mathcal{F}_{\frac{\Delta t}{2}}^x \circ \mathcal{F}_{\Delta t, \Delta x}^{\text{v}, \delta f}[\mathbf{W}_*^m, \mathbf{Z}^{n+\frac{1}{2}}] \circ \mathcal{F}_{\frac{\Delta t}{2}}^x \quad (30)$$

with split flows defined similarly as in (17)–(18) and a field solver adapted to the ansatz (1), namely

$$\mathcal{F}_{\Delta t, \Delta x}^{\text{v}, \delta f}[\mathbf{W}_*^m, \mathbf{Z}^{n+\frac{1}{2}}] : (x, v) \mapsto (x, v - \Delta t E^{n+\frac{1}{2}}(x)) \quad (31)$$

with

$$E^{n+\frac{1}{2}} = E_*^m + E_{\delta f}^{n+\frac{1}{2}} = \mathbf{E}_{\Delta x, h_*}[\mathbf{W}_*^m, \mathbf{Z}^{n+\frac{1}{2}}]. \quad (32)$$

Since both parts of the density are formally written as weighted collections of spline shapes, we may use a standard PIC solver (21) for each parts. The field induced by the bulk density f_*^m is

$$E_*^m := \mathbf{E}_{\Delta x, h_*}^{\text{pic}}[\mathbf{W}_*^m, \mathbf{Z}_*] \quad (33)$$

and the field corresponding to the variation $\delta f^{n+\frac{1}{2}} = \Phi_\varepsilon[\delta \mathbf{W}^{n+\frac{1}{2}}, \mathbf{Z}^{n+\frac{1}{2}}]$, with scaling $\varepsilon = \Delta x$, reads

$$E_{\delta f}^{n+\frac{1}{2}} = \mathbf{E}_{\Delta x}^{\text{pic}}[\delta \mathbf{W}^{n+\frac{1}{2}}, \mathbf{Z}^{n+\frac{1}{2}}] \quad \text{with} \quad \begin{cases} \delta \mathbf{W}^{n+\frac{1}{2}} := \delta \mathcal{W}(\mathbf{W}_*^m, \mathbf{Z}^{n+\frac{1}{2}}) \\ \mathbf{Z}^{n+\frac{1}{2}} := \mathcal{F}_{\frac{\Delta t}{2}}^x(\mathbf{Z}^n) \end{cases} \quad (34)$$

see (19), (29), (26). The resulting field solver corresponding to (32) may then be written as

$$\mathbf{E}_{\Delta x, h_*}[\mathbf{W}_*^m, \mathbf{Z}^{n+\frac{1}{2}}] := \mathbf{E}_{\Delta x, h_*}^{\text{pic}}[\mathbf{W}_*^m, \mathbf{Z}_*] + \mathbf{E}_{\Delta x}^{\text{pic}}[\delta \mathcal{W}(\mathbf{W}_*^m, \mathbf{Z}^{n+\frac{1}{2}}), \mathbf{Z}^{n+\frac{1}{2}}]. \quad (35)$$

Remark 4.1. *Since the field E_*^m is constant between two remappings, regular time steps only involve a deposition of the δf particles to update the $E_{\delta f}$ part. Note that even if $|\delta f^n| \ll |f_*^m|$, there is no reason why $E_{\delta f}$ should be small compared to E_*^m . In particular, we have $E_*^m \approx 0$ when f_*^m is close to an equilibrium density.*

4.3 FBL remappings with auxiliary markers

For the remappings, namely the updates of the bulk density $f_*^{\hat{m}} \mapsto f_*^m$ with $m = \hat{m} + N_r$, we resort to Forward-Backward Lagrangian (FBL) reconstructions [4]. As mentioned above this involves a collection of auxiliary markers that have been reset on the cartesian grid at the previous remapping step,

$$\tilde{\mathbf{Z}}^{\hat{m}} := \mathbf{Z}_*, \quad \text{i.e.,} \quad \tilde{z}_j^{\hat{m}} := \mathbf{j}h_* \quad \forall \mathbf{j} \in \mathbb{Z}^d, \quad (36)$$

and pushed forward similarly as the classical ones in (25),

$$\tilde{\mathbf{Z}}^m = \mathcal{F}^{m-1}(\dots \mathcal{F}^{\hat{m}}(\mathbf{Z}_*) \dots) \quad (37)$$

in order to track the forward characteristic flow. The FBL method then performs a semi-Lagrangian step

$$f_*^m := A_* \mathcal{T}_{\text{fbl}}[\tilde{\mathbf{Z}}^m] f_*^{\hat{m}} \quad \text{with} \quad \hat{m} = m - N_r \quad (38)$$

where A_* is a spline interpolation or quasi-interpolation operator on the h_* grid, and $\mathcal{T}_{\text{fbl}}[\tilde{\mathbf{Z}}^m] : f \rightarrow f \circ \mathcal{B}_{\text{fbl}}^{\hat{m},m}$ is a transport operator approximating (10), based on an FBL backward flow

$$\mathcal{B}_{\text{fbl}}^{\hat{m},m} = \mathcal{B}_{\text{fbl}}[\tilde{\mathbf{Z}}^m] \approx \mathcal{B}_{\text{ex}}^{\hat{m},m}. \quad (39)$$

As a result we obtain a numerical scheme to update the coefficients of the bulk density, which we summarize as

$$\mathbf{W}_*^m := \text{Remap}[\tilde{\mathbf{Z}}^m](\mathbf{W}_*^{\hat{m}}) \quad \text{where} \quad \hat{m} = m - N_r. \quad (40)$$

In the next subsection we give some details about the FBL algorithm.

4.4 FBL density reconstructions

The FBL scheme (38) performs a semi-Lagrangian approximation with a backward flow derived from the position of the auxiliary markers $\tilde{\mathbf{Z}}^m$ in (37), as follows:

- (i) for any index $\mathbf{j} \in \mathbb{Z}^d$, let \tilde{z}_i^m with $\mathbf{i} = \mathbf{i}(\mathbf{j})$ be an FBL marker close to the node $\mathbf{j}h_*$
- (ii) compute the quadratic local backward flow associated with \tilde{z}_i^m , namely

$$B_i^{\hat{m},m}(z) = z_i^* + D_i^m(z - \tilde{z}_i^m) + \frac{1}{2}(z - \tilde{z}_i^m)^T Q_i^m(z - \tilde{z}_i^m) \quad \text{with} \quad z_i^* = \mathbf{i}h_* \quad (41)$$

where D_i^m and Q_i^m correspond respectively to the Jacobian matrix and Hessian tensor of the backward flow at $z = \tilde{z}_i^m$, computed from the positions of the logical neighbors of \tilde{z}_i^m (for more details we refer to [4])

- (iii) reconstruct the transported density at node $\mathbf{j}h_*$ using this approximated flow,

$$f_{*,\mathbf{j}}^m := f_*^{\hat{m}}(B_i^{\hat{m},m}(z_j^*)) \quad (42)$$

(iv) compute the new weights \mathbf{W}_*^m using a spline approximation operator A^* .

For the operator A_* , we can use a standard interpolation scheme, or even a local quasi-interpolation schemes, see e.g. [7]. Both compute high-order B-spline approximations, but the later only involves local pointwise evaluations of the target function. The resulting approximation takes the form

$$A_*g(z) := \sum_{\mathbf{j} \in \mathbb{Z}^d} w_{\mathbf{j}}(g) \varphi_{h_*}(z - \mathbf{j}h_*) \quad \text{with} \quad w_{\mathbf{j}}(g) := h_*^d \sum_{\|\mathbf{i}\|_\infty \leq m_p} a_{\mathbf{i}} g((\mathbf{j} + \mathbf{i})h_*), \quad (43)$$

with coefficients $a_{\mathbf{i}} := a_{i_1} \cdots a_{i_d}$ given by the symmetric method ($a_{\mathbf{i}} = a_{-\mathbf{i}}$) in [7, Sec. 6]. For the first odd orders we have

- $m_p = 0$ and $a_0 = 1$ for $p = 1$,
- $m_p = 1$ and $(a_0, a_1) = (\frac{8}{6}, -\frac{1}{6})$ for $p = 3$,
- $m_p = 4$ and $(a_0, a_1, a_2, a_3, a_4) = (\frac{503}{288}, -\frac{1469}{3600}, \frac{7}{225}, \frac{13}{3600}, \frac{1}{14400})$ for $p = 5$.

5 Overview of the δf particle scheme with FBL remappings

Gathering the above steps, we may write the solution at time t^n as

$$f^n = f_*^m + \delta f^n \quad \text{with} \quad \begin{cases} f_*^m = \Phi_{h_*}[\mathbf{W}_*^m, \mathbf{Z}_*] \\ \delta f^n = \Phi_\varepsilon[\delta \mathbf{W}^n, \mathbf{Z}^n]. \end{cases} \quad (44)$$

Here we remind that $\mathbf{Z}_* = (\mathbf{j}h_*)_{\mathbf{j} \in \mathbb{Z}^d}$ are the coarse grid nodes and $m = m(n)$ is the last remapping step preceding n , see (24). The proposed scheme reads then as follows.

5.1 Initialization

- compute the weights \mathbf{W}_*^0 of the initial bulk density $f_*^0 = \Phi_{h_*}[\mathbf{W}_*^0, \mathbf{Z}_*]$ with

$$f_*^0 := A_*f^0$$

using a spline approximation scheme such as (43),

- draw the δf markers according to some initial sampling distribution

$$\mathbf{Z}^0 \sim g^0$$

- and initialize the auxiliary FBL markers on the h_* grid (36),

$$\tilde{\mathbf{Z}}^0 = \mathbf{Z}_* .$$

5.2 Time loop

For $n = 0, \dots, N_t - 1$, let $m := \lfloor \frac{n}{N_r} \rfloor N_r$ denote the previous remapping step as in (24), and do:

- if $n = m > 0$, **remap**:

▷ update the bulk density weights (coefficients) with the FBL method described in Section 4.4,

$$\mathbf{W}_*^m := \text{Remap}[\tilde{\mathbf{Z}}^m](\mathbf{W}_*^{\hat{m}}) \quad (45)$$

▷ reset the FBL markers with (36), $\tilde{\mathbf{Z}}^m := \mathbf{Z}_*$

- **Push** the markers forward:

$$\begin{cases} \mathbf{Z}^{n+1} := \mathcal{F}^n(\mathbf{Z}^n) \\ \tilde{\mathbf{Z}}^{n+1} := \mathcal{F}^n(\tilde{\mathbf{Z}}^n) \end{cases} \quad (46)$$

using some discrete flow $\mathcal{F}^n = \mathcal{F}_{\Delta t}^{\delta f}[\mathbf{W}_*^m, \mathbf{Z}^n]$ such as the leap-frog scheme (30), which involves deposition and field solver steps as detailed in Section 4.2 and 3.5.

5.3 FBL variant

A semi-Lagrangian FBL variant of the above scheme can be obtained by (i) setting $N_p = 0$ and (ii) treating the FBL markers $\tilde{\mathbf{Z}}^n$ as “active” particles in the field solver.

Specifically, this amounts to discarding the δf part ($\mathbf{Z}^n = \emptyset$) so that the full density is represented on the structured spline grid on the successive remapping steps, and to defining the electric field in (30)–(31) by

$$E^{n+\frac{1}{2}} = \mathbf{E}_{\Delta x}^{\text{pic}}[\mathbf{W}_*^{n+\frac{1}{2}}, \tilde{\mathbf{Z}}^{n+\frac{1}{2}}] \quad (47)$$

as one would do with a standard full- f PIC scheme, see (18)–(20), using the weighted FBL markers as standard particles. Note that here the weights are those set at the last remapping step (45), i.e. $\mathbf{W}_*^{n+\frac{1}{2}} = \mathbf{W}_*^m$ with m as in (24).

6 Numerical results

In this section we assess the proposed method on the periodic 1D1V Vlasov-Poisson system (11)–(12), where we compare it with other PIC and semi-Lagrangian schemes.

6.1 Numerical parameters for the tested methods

For the purpose of comparison, we use different values for the main parameters listed in Section 2.1, including some limiting values which allows to emulate full- f and δf PIC schemes, as well as a semi-Lagrangian FBL scheme. All the methods use cubic splines for the particle shape functions.

As the solutions are typically supported in a region occupying roughly one half of the computational phase-space domain, for each grid resolution $N_x \times N_v$ we indicate as $N_*^{\text{eff}} \approx N_*/2$, with $N_* = N_x N_y$, the approximate number of active spline coefficients on the grid, corresponding to the “effective” grid resolution. The resulting methods are summarized in Table 1.

Table 1: Numerical parameters used for the different methods, as described in the text.

method	N_p	grid (FBL)	N_*^{eff}	N_r	FBL markers
full- f PIC (coarse)	20,000	0×0	0	∞	\emptyset
full- f PIC (fine)	320,000	0×0	0	∞	\emptyset
δf PIC	18,752	50×50	1,250	∞	frozen
FBL (coarse)	0	200×200	20,000	20	active
FBL (fine)	0	800×800	320,000	20	active
FBL- δf PIC	18,752	50×50	1,250	20	passive

Here the active/passive/frozen status of FBL markers $\tilde{\mathbf{Z}}^n$ refers to their role in the scheme and in particular in the field solver that is involved in the push step (46): *active* markers (used in the FBL variant) carry a charge which is deposited as explained in Section 5.3 while *passive* markers (used in the proposed FBL- δf scheme) do not, as described in Section 4.2. Finally *frozen* markers are passive, and never pushed: in the absence of remappings only their initial position on the grid is used to represent the bulk density $f_*^n = f_*^0$.

6.2 Test cases

Our numerical experiments are based on a 1D1V two-stream instability test case where the initial distribution is of the form

$$f^0(x, v) = (1 + \alpha \cos(kx)) \frac{v^2}{\sqrt{2\pi}} e^{-\frac{v^2}{2}} \quad (48)$$

with a wave number of $k = \frac{1}{2}$ and a perturbation amplitude of $\alpha = 0.01$. This solution is known to develop thin filaments in the phase space that are difficult to resolve numerically, see e.g. [6, 16]. Here we will simulate two-stream instabilities on the time interval $[0, 100]$. We shall consider two versions of the problem:

- (i) the basic Two-Stream Instability (TSI) test case where the solution is evolved with the self-consistent Vlasov-Poisson system (11)–(12)
- (ii) a Driven Two-Stream Instability (D-TSI) test case where an oscillating external field

$$E_{\text{ext}}(t, x) = \frac{1}{10} \cos\left(\frac{\pi t}{50}\right) \quad (49)$$

is added to the self-consistent field (12). The effect of this external drive is to add a periodic perturbation to the TSI trajectories, uniform in x and v ,

$$(x, v) \mapsto \left(x + \frac{250}{\pi^2} \left(1 - \cos\left(\frac{\pi t}{50}\right) \right), y + \frac{5}{\pi} \sin\left(\frac{\pi t}{50}\right) \right),$$

so that the solutions to both test cases coincide for $t = 100$.

The computational phase-space domain is set to $\Omega = [0, \frac{2\pi}{k}] \times [-v_{\max}, v_{\max}]$ with $v_{\max} = 10$. Note that this value is significantly larger than what is usually seen in the literature, in order to correctly represent the variations in velocity induced by the oscillating drive. Finally the initial sampling distribution for the particles is taken as $g^0 = (\int f^0(z) dz)^{-1} f^0$ for the full- f PIC scheme, and as

$$g^0(x, v) = \frac{1}{L_x} \frac{1}{\sigma \sqrt{2\pi}} e^{-\frac{v^2}{2\sigma^2}} \quad (50)$$

with $L_x = \frac{2\pi}{k}$ and $\sigma = 2$, for the δf and FBL- δf PIC methods.

6.3 Phase-space density plots

In Figures 1 and 2, we plot the densities f^n corresponding to the different methods listed in Table 1 for both the TSI and D-TSI test cases, at the time $t^n = 100$ where the exact solutions coincide.

For both test cases we observe very noisy (oscillating) profiles for the coarse full- f PIC solutions which use about 20,000 particles, and smoother profiles for the fine PIC solutions which use 16 times as many particles. FBL solutions are essentially free of spurious oscillations, with many fine structures well resolved in the fine solutions compared to the coarse ones. We also note that the TSI and D-TSI solutions are in very good agreement at $t^n = 100$ for these full- f numerical simulations.

Regarding the δf solutions, we observe that in the TSI test case (Fig. 1) both the basic δf PIC and the FBL- δf PIC methods allow to strongly reduce the level of oscillations compared to the coarse PIC simulation – all three using approximately 20,000 ‘active’ particles. In the D-TSI case however (Fig. 2), we see a significant reduction in the accuracy of the basic δf solution, where the global central vortex suffers from a visible deterioration and spurious streams of particles have appeared at high-velocities. In contrast, the accuracy of the FBL- δf PIC method remains very comparable to that of the TSI case.

To better visualize the difference in the two methods, we next show in Figures 3 to 8 a series of plots corresponding to snapshots of various densities at successive times $t^n = 0, 12.5, \dots, 87.5$ for the D-TSI test case: In Figure 3 and 4 we show the evolution of the δf and FBL- δf solutions, completed by that of a reference scheme (an FBL simulation using a 1024×1024 grid) in Figure 5. In Figure 6 we then show the evolution of the bulk density f_*^n computed by the FBL- δf PIC method, which we remind is periodically remapped on a 50×50 grid of cubic splines, see Table 1. Finally the evolution of the residual δf^n densities are shown in Figure 7 for the basic δf method, and in Figure 8 for the FBL- δf method.

From these plots we see that the density strongly deviates from its initial value due to the external drive, which clearly challenges the basic assumption of a standard δf approach. Here, we have chosen a deviation so large that the bulk density cannot be compensated by a proper δf weighting of the particles, leading to significant errors in the full f^n density visible in Figure 3. As expected the solution computed with the FBL- δf PIC method on Fig. 4 does not show this erratic behaviour. The main reason for this is visible in Fig. 6 where we see that the coarse bulk density computed by the FBL- δf scheme properly follows the total density. As a result the δf particles can effectively represent small scale variations with respect to the main part of the plasma density, which is made evident in Fig. 7 and 8, where we see that the amplitude of the δf weights is strongly reduced in the FBL- δf scheme, as compared with the basic approach.

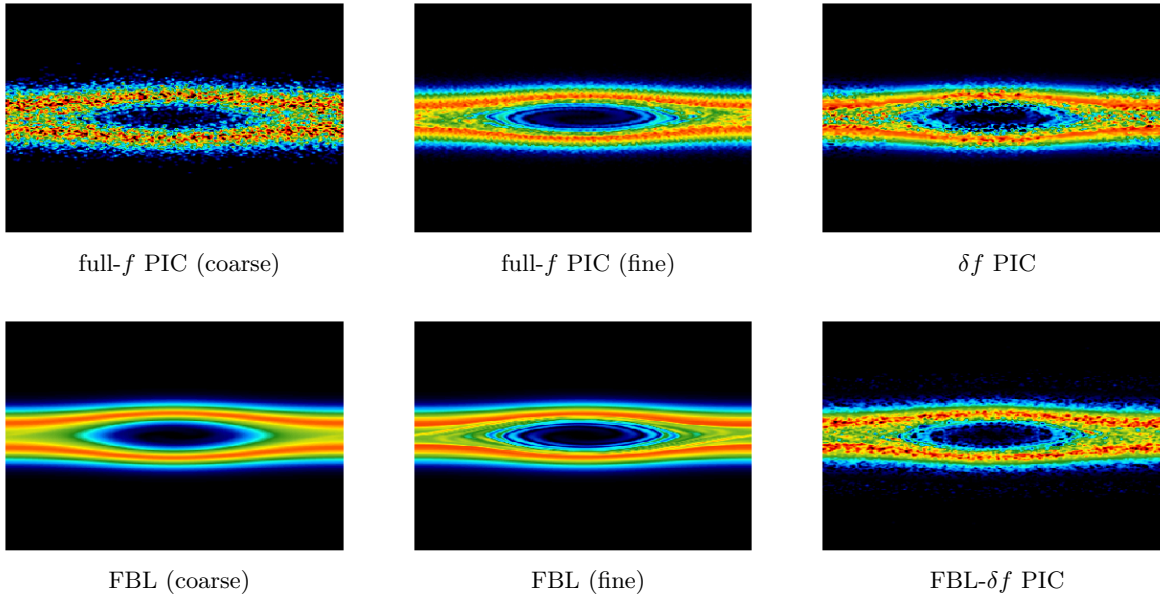


Figure 1: Phase-space densities f^n obtained for the TSI test case at $t^n = 100$ with the methods listed in Table 1. Here the basic δf and FBL- δf methods use about 18,750 standard particles and 1,250 FBL markers, which is comparable to the 20,000 particles (or active markers) used in the coarse PIC and FBL methods. Fine PIC and FBL simulations use 16 as many particles.

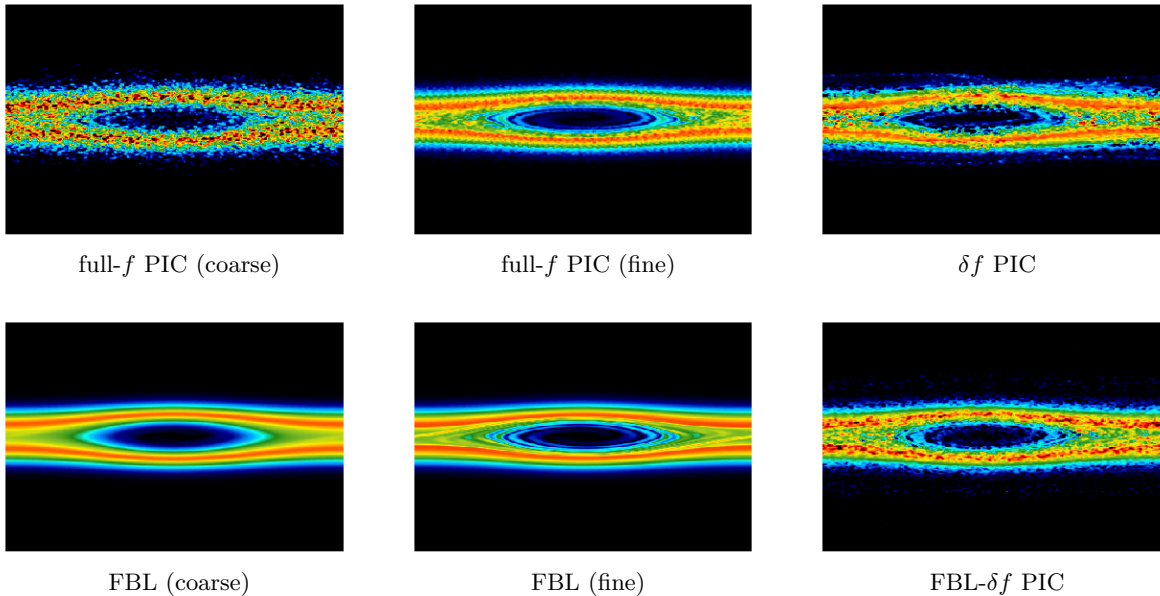


Figure 2: Densities obtained for the D-TSI test case at $t^n = 100$, where the exact solution coincides with the TSI one. As in Fig. 1, the different methods are those listed in Table 1.

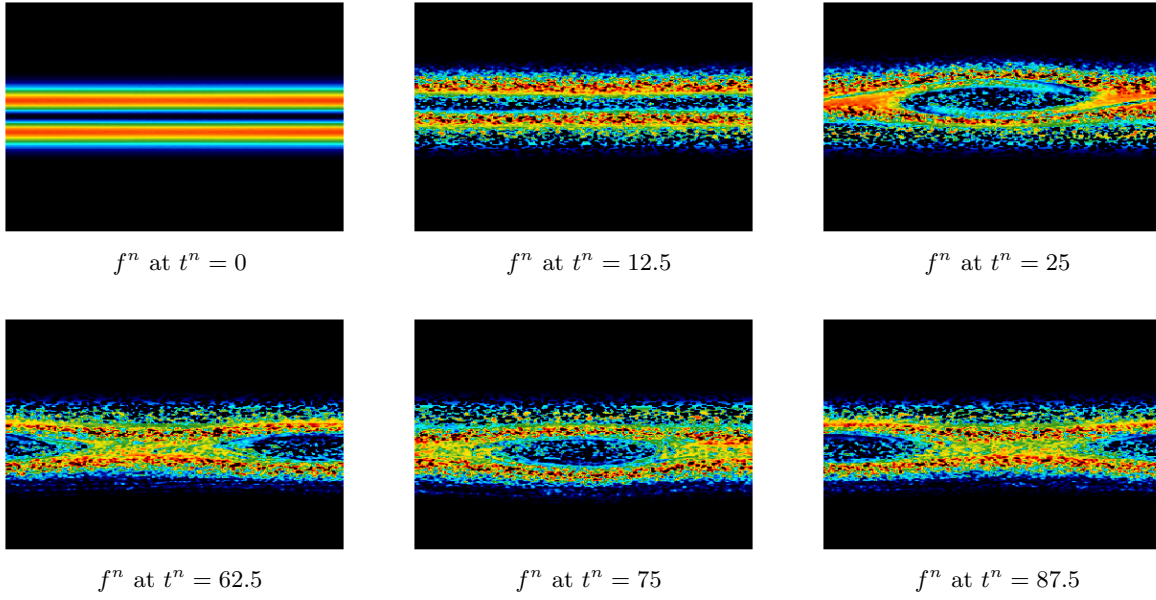


Figure 3: Snapshots of the density f^n computed by the δf PIC scheme at various times t^n , for the D-TSI test case. At time $t^n = 100$, the corresponding density is shown in the upper-right plot of Fig. 2.

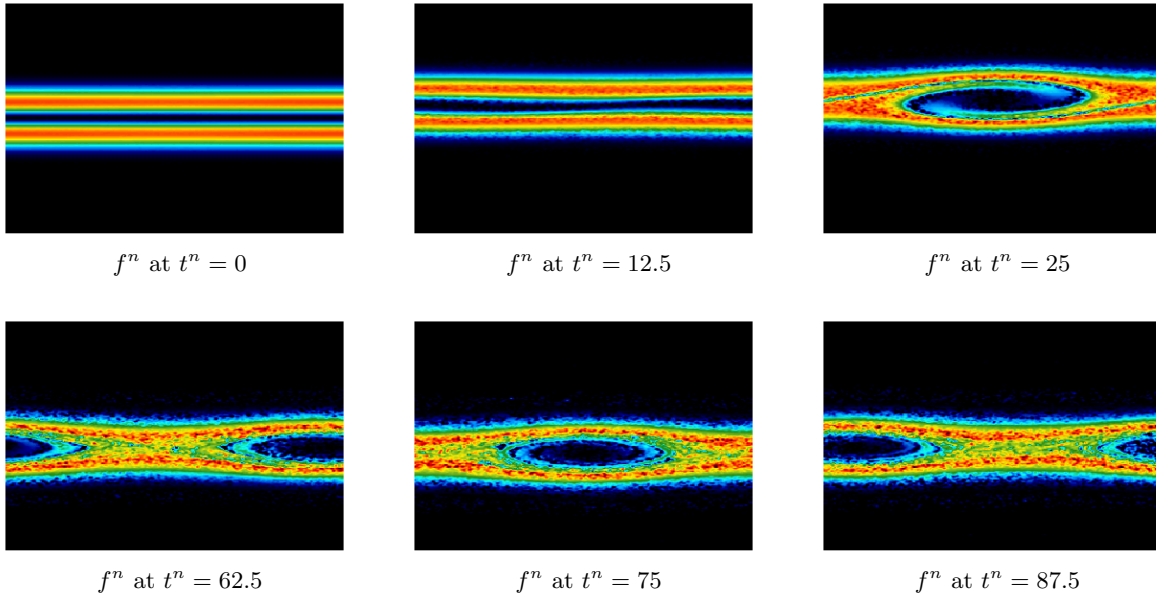


Figure 4: Snapshots of the density f^n computed by the FBL- δf PIC scheme at various times t^n , for the D-TSI test case. At time $t^n = 100$, the corresponding density is shown in the lower-right plot of Fig. 2.

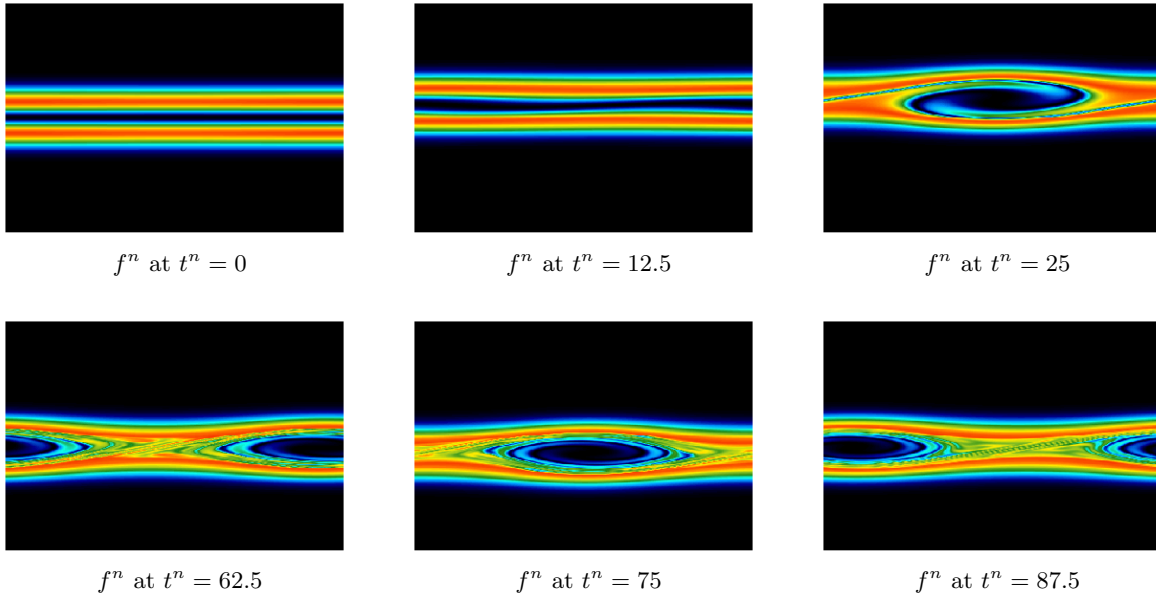


Figure 5: Snapshots of the density f^n obtained with a reference method for the same times than in Figures 3 and 4, again for the D-TSI test case.

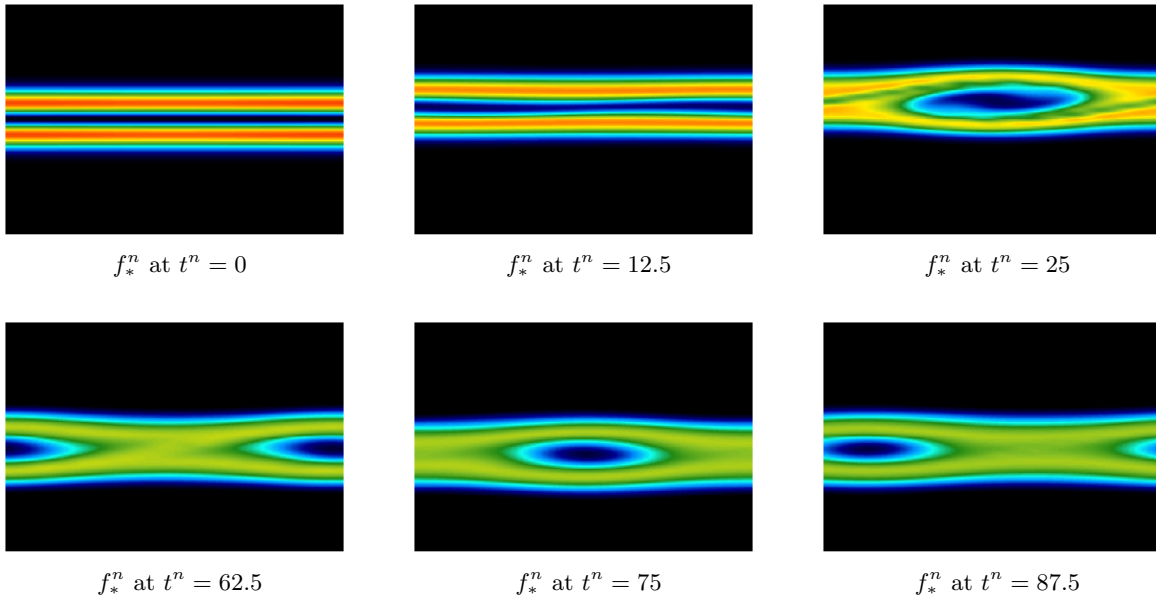


Figure 6: Snapshots of the bulk density f_*^n corresponding to the FBL- δf PIC simulation shown in Figure 4.

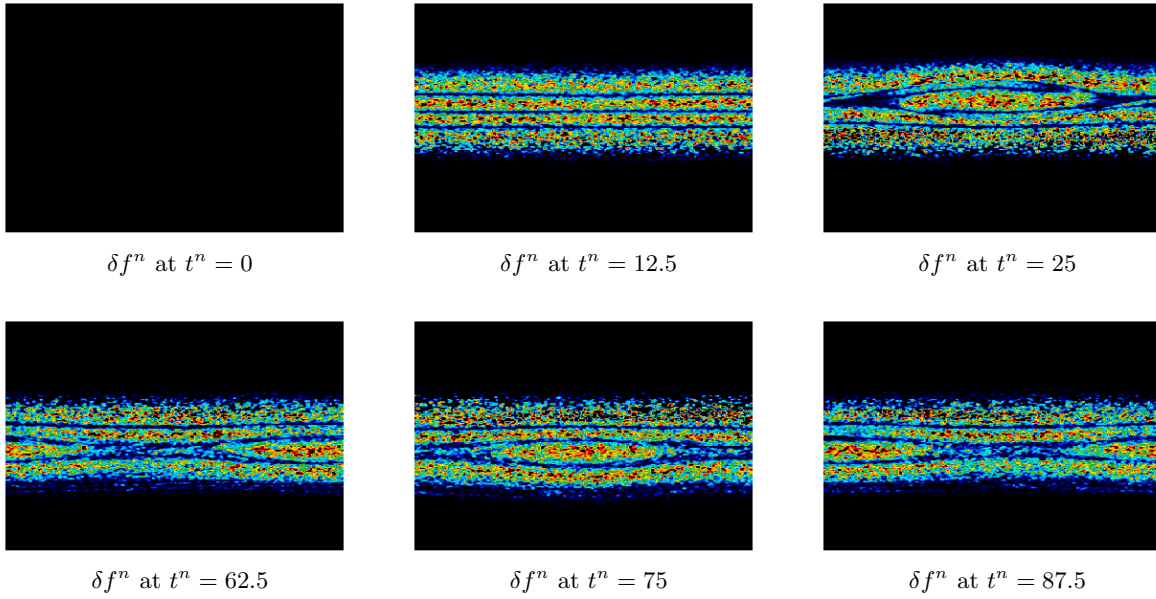


Figure 7: Snapshots of the residual density δf^n corresponding to the δf PIC simulation shown in Figure 3.

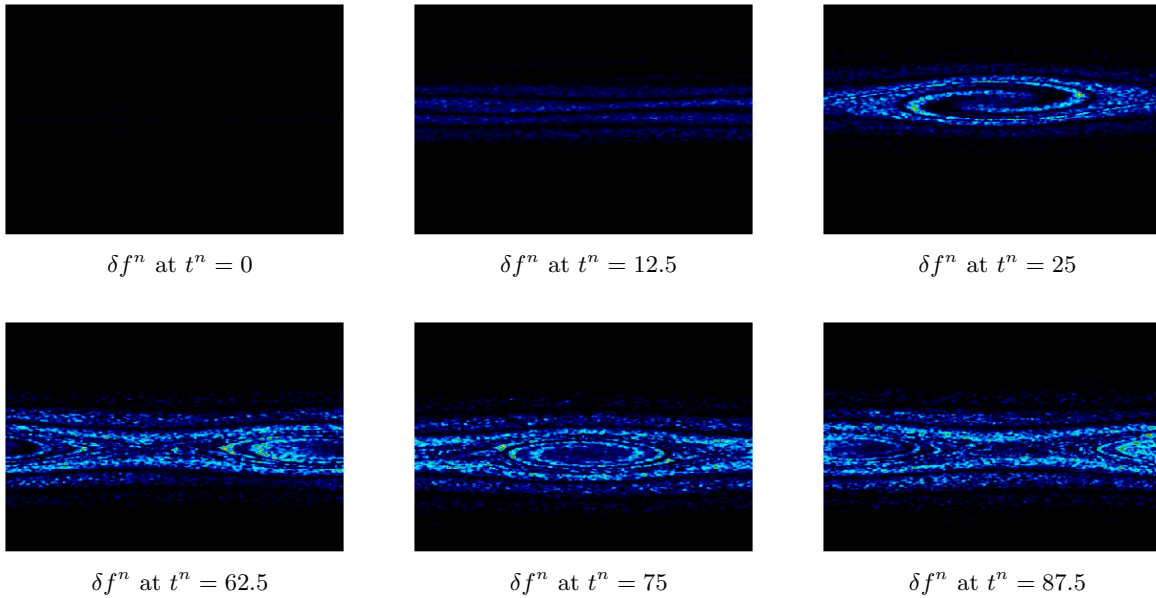


Figure 8: Snapshots of the residual density δf^n corresponding to the FBL- δf PIC simulation shown in Figure 4.

6.4 Density and field plots in physical space

In Figures 9 and 10 we next plot the snapshots of the deposited charge densities ρ^n for the D-TSI test case, corresponding to the δf and FBL- δf solutions shown in in Figures 3 and 4. For a better assessment of the accuracy, we also plot in dashed line a reference charge density computed by a fine semi-Lagrangian scheme. The associated E^n fields are plotted in Figures 11 and 12.

These plots show that despite the velocity averaging, the high level of noise visible in the phase-space densities is also present in the deposited charge densities, which results in significant errors in the self-consistent electric field.

6.5 Reduction of the statistical errors

We conclude our numerical experiments by considering the empirical variances for the total particle number and current, as defined by Equations (4.80) and (4.81) in [9], namely

$$\sigma_N^2 = \frac{N_p^2}{N_p - 1} \left[\sum_{k=1}^{N_p} (\delta w_k)^2 - \left(\sum_{k=1}^{N_p} \delta w_k \right)^2 \right] \quad (51)$$

and

$$\sigma_J^2 = \frac{N_p^2}{N_p - 1} \left[\sum_{k=1}^{N_p} (v_k \delta w_k)^2 - \left(\sum_{k=1}^{N_p} v_k \delta w_k \right)^2 \right] \quad (52)$$

respectively. Here we note that here the weight normalisation in (26), $\delta w_k \approx \frac{1}{N_p} \frac{\delta f(z_k)}{g(z_k)}$, differs from that of [9], and for a full- f scheme the weights are $w_k = \frac{1}{N_p} \frac{f(z_k)}{g(z_k)}$. In particular we have $\sigma_N = 0$ in the case of a sampling with probability distribution $g^0 = f^0 / (\int f^0(z) dz)$.

Following the interpretation of the δf method as a variance reduction technique [2], these respective quantities may be used as quantitative indicators of the statistical errors associated with the Monte Carlo approximation of the total density $\iint f(t, x, v) dx dv$ and normalized current $\iint f(t, x, v) v dx dv$, see [9, Sec. 2].

In Figure 13, we plot these quantities for the two test cases, and for the three coarse PIC schemes, namely the coarse full- f PIC, the basic δf and the FBL- δf scheme. For the TSI test case corresponding to the top plots, we observe that the δf schemes indeed result in a reduction of the current variance σ_J , of a factor between two and three (the full- f density variance is zero as previously noticed). We also note a secular growth in the case of the FBL- δf scheme, which is maybe due to the slow diffusion of the bulk density caused by the periodic remappings.

For the D-TSI test case, we observe similar values for the current variances σ_J of the full- f FBL- δf PIC simulations (with values around 20 and 10, respectively). In contrast, strong oscillations are visible in the variances of the basic δf PIC scheme, which are closely correlated with the deviation in velocity already seen in Figure 3, and the associated offset with the initial density. The amplitude of these oscillations (around 40) confirm our previous observations that a basic δf approach is no longer justified when the density deviates significantly from its initial profile, and further validates the proposed method in such regimes.

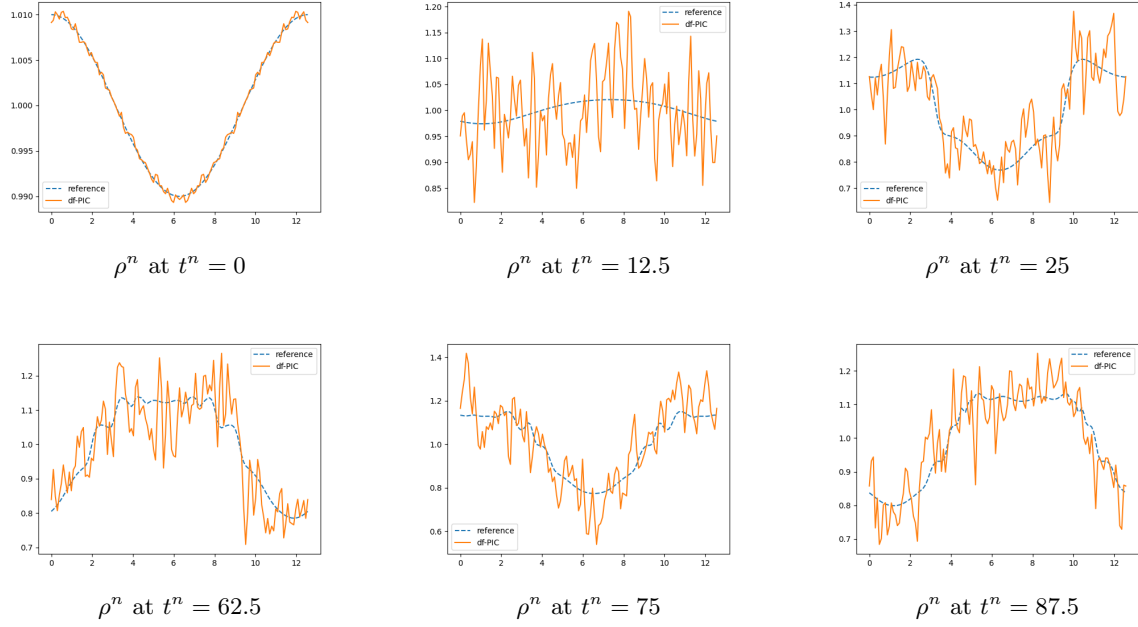


Figure 9: Snapshots of the charge density ρ^n deposited with the δf PIC scheme (with the D-TSI test case), corresponding to the phase-space densities shown in Figure 3.

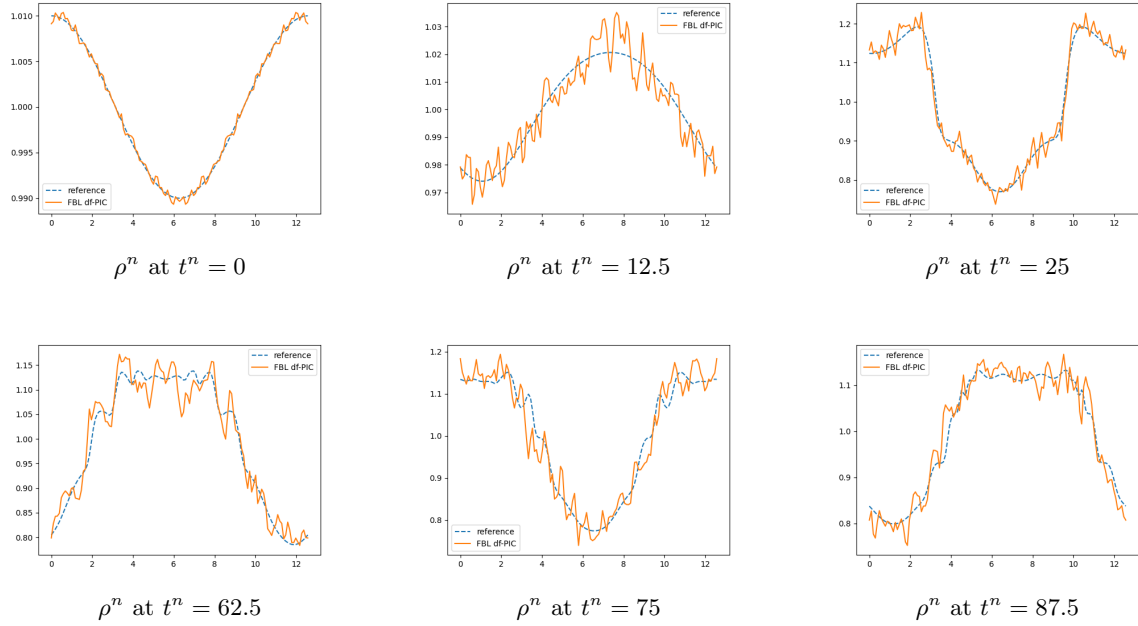


Figure 10: Snapshots of the charge density ρ^n deposited with the FBL- δf PIC scheme (with the D-TSI test case), corresponding to the phase-space densities shown in Figure 4.

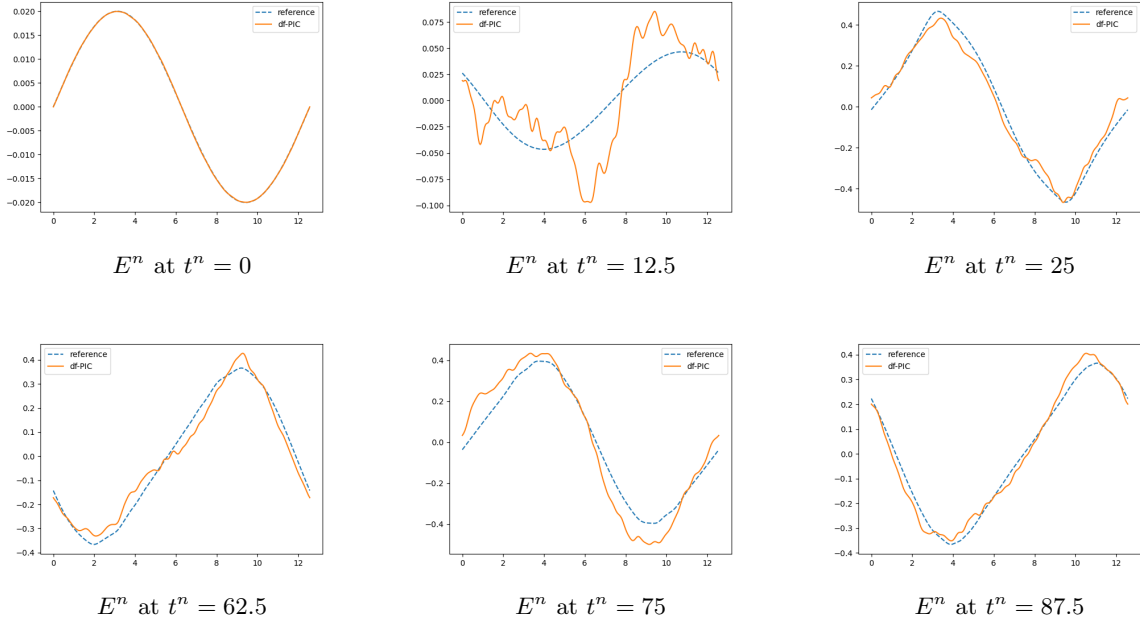


Figure 11: Snapshots of the self-consistent field E^n computed by the δf PIC scheme (D-TSI), corresponding to the charge densities shown in Figure 9.

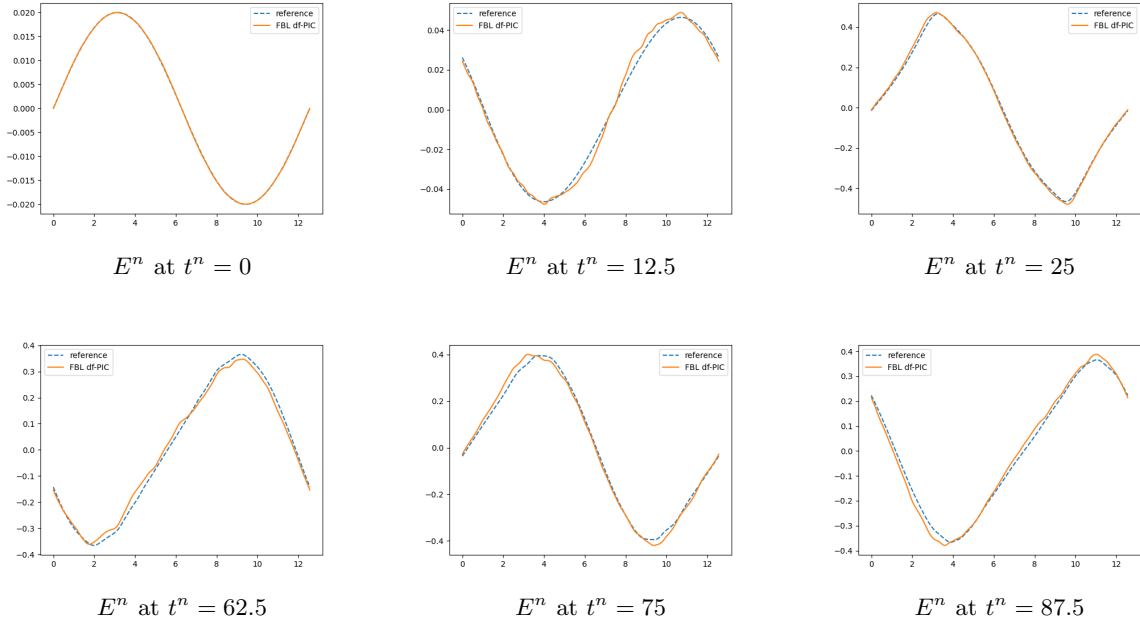


Figure 12: Snapshots of the self-consistent field E^n computed by the FBL- δf PIC scheme (D-TSI) corresponding to the charge densities shown in Figure 10.

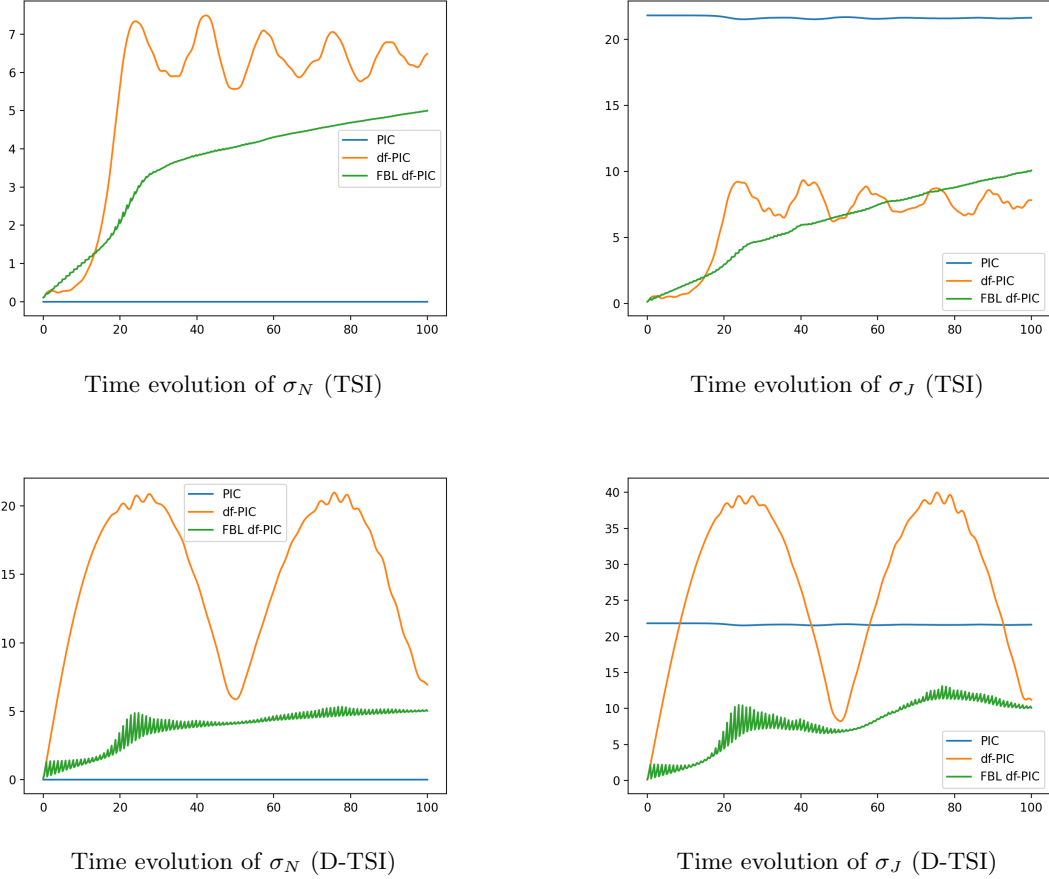


Figure 13: Time evolution of the empirical variances for the TSI (top row) and D-TSI (bottom row) test cases.

Acknowledgement

This work has been carried out within the framework of the EUROfusion Consortium, funded by the European Union via the Euratom Research and Training Programme (Grant Agreement No 101052200 – EUROfusion). Views and opinions expressed are however those of the authors only and do not necessarily reflect those of the European Union or the European Commission. Neither the European Union nor the European Commission can be held responsible for them.

References

- [1] S J Allfrey and R Hatzky. A revised δf algorithm for nonlinear pic simulation. *Computer Physics Communications*, 154(2):98–104, Aug 2003.
- [2] A. Y. Aydemir. A unified monte carlo interpretation of particle simulations and applications to non-neutral plasmas. *Physics of Plasmas*, 1(4):822–831, April 1994.

- [3] C K Birdsall and A.B. Langdon. *Plasma physics via computer simulation*. Adam Hilger, IOP Publishing. Adam Hilger, IOP Publishing, 1991. Original Version: McGraw-Hill, New York, 1985.
- [4] Martin Campos Pinto and Frédérique Charles. From particle methods to forward-backward Lagrangian schemes. *SMAI Journal of Computational Mathematics*, 4:121–150, 2018.
- [5] Yang Chen and Scott E Parker. Coarse-graining phase space in δf particle-in-cell simulations. *Physics of Plasmas*, 14(8):2301, August 2007.
- [6] C Z Cheng and G Knorr. The integration of the vlasov equation in configuration space. *Journal of Computational Physics*, 22:330–351, Nov 1976.
- [7] C.K. Chui and H. Diamond. A characterization of multivariate quasi-interpolation formulas and its applications. *Numerische Mathematik*, 57(1):105–121, 1990.
- [8] A. M. Dimits and W. W. Lee. Partially linearized algorithms in gyrokinetic particle simulation. *Journal of Computational Physics*, 107(2):309–323, 1993.
- [9] R. Hatzky, R. Kleiber, A. Könies, A. Mishchenko, M. Borchardt, A. Bottino, and E. Sonnendrücker. Reduction of the statistical error in electromagnetic gyrokinetic particle-in-cell simulations. *Journal of Plasma Physics*, 85(1):905850112, Feb 2019.
- [10] Roman Hatzky, Trach Minh Tran, Axel Könies, Ralf Kleiber, and Simon J. Allfrey. Energy conservation in a nonlinear gyrokinetic particle-in-cell code for ion-temperature-gradient-driven modes in θ -pinch geometry. *Physics of Plasmas*, 9(3):898–912, 2002.
- [11] M. Kotschenreuther. Numerical simulation. In *Bulletin of the American Physical Society*, volume 33, page 2017, 1988.
- [12] A. Mishchenko, A. Bottino, R. Hatzky, E. Sonnendrücker, R. Kleiber, and A. Könies. Mitigation of the cancellation problem in the gyrokinetic particle-in-cell simulations of global electromagnetic modes. *Physics of Plasmas*, 24(8):081206, Aug 2017.
- [13] Alexey Mishchenko, Roman Hatzky, and Axel Könies. Conventional δf -particle simulations of electromagnetic perturbations with finite elements. *Physics of Plasmas*, 11(12):5480–5486, 2004.
- [14] S. E. Parker and W. W. Lee. A fully nonlinear characteristic method for gyrokinetic simulation. *Physics of Fluids B: Plasma Physics*, 5(1):77–86, 1993.
- [15] P.-A. Raviart. An analysis of particle methods. In *Numerical methods in fluid dynamics (Como, 1983)*, pages 243–324. Lecture Notes in Mathematics, Berlin, 1985.
- [16] James A Rossmanith and David C Seal. A positivity-preserving high-order semi-Lagrangian discontinuous Galerkin scheme for the Vlasov-Poisson equations. *Journal of Computational Physics*, 230(16):6203 – 6232, 2011.
- [17] E. Sonnendrücker, J. Roche, P. Bertrand, and A. Ghizzo. The semi-Lagrangian method for the numerical resolution of the Vlasov equation. *Journal of Computational Physics*, 149(2):201–220, 1999.

- [18] E. Sonnendrücker, Abigail Wachter, Roman Hatzky, and Ralf Kleiber. A split control variate scheme for PIC simulations with collisions. *Journal of Computational Physics*, 295:402–419, August 2015.
- [19] T. Vernay, S. Brunner, L. Villard, B. F. McMillan, S. Jolliet, T. M. Tran, A. Bottino, and J. P. Graves. Neoclassical equilibria as starting point for global gyrokinetic microturbulence simulations. *Physics of Plasmas*, 17(12):122301, 2010.